**THE EUROPEAN
PHYSICAL JOURNAL E**

Regular Article

Dynamics at the air-water interface revealed by evanescent wave light scattering

A. Stocco[1,a], K. Tauer[1], S. Pispas[2], and R. Sigel[3,b]

[1] Max Planck Institute of Colloids and Interfaces, 14476 Golm, Germany
[2] Theoretical and Physical Chemistry Institute, National Hellenic Research Foundation, 48 Vass. Constantinou Ave., 11635 Athens, Greece
[3] Adolphe Merkle Institute, University Fribourg, Chemin du Musée 3, Perolles, CH-1700 Fribourg, Switzerland

Abstract. A new tool to study surface phenomena by evanescent wave light scattering is employed for an investigation of an aqueous surface through the water phase. When the angle of incidence passes the critical angle of total internal reflection, a high and narrow scattering peak is observed. It is discussed as an enhancement of scattering at critical angle illumination. Peak width and height are affected by the interfacial profile and the focusing of the beam. In addition, the propagation of capillary waves was studied at the surface of pure water and in the presence of latex particles and amphiphilic diblock copolymers. The range of the scattering vectors where propagating surface waves were detected is by far wider than standard surface quasi-elastic light scattering (SQELS) and comparable with those of X-ray photon correlation spectroscopy (XPCS).

PACS. 68.03.-g Gas-liquid and vacuum-liquid interfaces – 68.03.Kn Dynamics (capillary waves) – 68.35.bm Polymers, organics

1 Introduction

The free surface of a liquid medium is not perfectly flat. The interfacial density profile can deviate significantly from a step function because of either modified local molecular packing at the surface or due to surface roughness, *i.e.* capillary waves driven by thermal excitation [1]. These capillary waves can be described by hydrodynamic equations [2] and tend to disappear under the influence of gravity and capillarity forces.

The exact description of the density profile along fluid interfaces is still a matter of discussion. Several authors report discrepancies between theoretically predicted interfacial profiles and experimental observations. Beaglehole described the anomalous behavior of the water surface under the effect of heating cycle, suggesting the existence of a denser water layer at the surface [3]. Meunier tried to couple the roughness due to capillary waves with a classical intrinsic interfacial profile, reporting inconsistencies [4]. Recently, an ellipsometric study at oil-water interfaces pointed out the effect of repulsive oil-water interactions at the interface [5]. In spite of the experimental and the-

oretical efforts, there is a lack of quantitative explanation of the phenomena taking place at fluid interfaces.

Light scattering is an established technique for investigation of soft matter systems in bulk or in solution [6]. Local fluctuations in the density, the concentration or the molecular orientation create fluctuations in the local dielectric constant, which cause light scattering. In dynamic light scattering (DLS), the evolution of such fluctuations is characterized by an autocorrelation function. It contains information about particle diffusion constants or relaxation times. The total magnitude of the scattered intensity detected in static light scattering (SLS), on the other hand, is determined by the thermal fluctuation amplitude. In dilute systems, the form factor, the molecular weight and the second virial coefficient of scattering particles are determined by SLS. Thermal fluctuations at an interface are the capillary waves. Again, SLS is determined by their amplitude, while DLS yields details of relaxation and propagation.

Up to now, capillary wave phenomena at the air-water interface were mainly studied in the accessible scattering vector range $0.01 < q$ (μm^{-1}) < 0.2 of surface quasi-elastic light scattering (SQELS), and recently by surface X-ray photon correlation spectroscopy (XPCS) [7]. Advances in the understanding of capillary wave phenomena by SQELS investigations were reviewed in Langevin's

---

[a] e-mail: antonio.stocco@mpikg.mpg.de
[b] e-mail: reinhard.sigel@unifr.ch
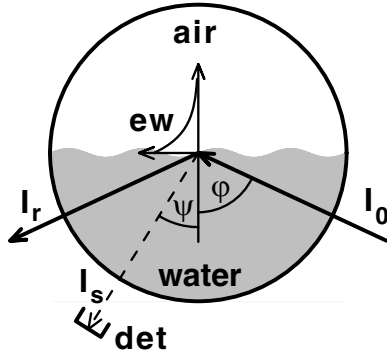
Fig. 1. Sketch of the cylindrical scattering cell. The light of intensity I_0 hits the interface with an angle of incidence φ which is larger than the critical angle of total internal reflection and an evanescent wave builds up in air. The scattering of intensity I_s is detected under the angle ψ.

monograph [1], by Earnshaw [8] and Cicuta [9]. The surface tension γ, the dilatational modulus ϵ', and the dilatational viscosity ϵ'' can be extracted by using a dispersion relation, which describes both the dilatational (in-plane) and transverse waves [10]. The transverse contribution strongly dominates the intensity in SQELS. New impulses in the theoretical and experimental description of capillary waves and surface phenomena came from X-ray photon correlation spectroscopy [7,11,12]. Mora and Daillant describe the existence of four modes affecting the liquid displacement at the interface [11]: two independent transverse modes (shear waves), a longitudinal mode for heat diffusion and an acoustic longitudinal mode.

A transition from propagating to over-damped waves is expected at a critical scattering vector q_{cr} [11]. Experimentally, this transition was observed in XPCS experiments by decreasing the temperature in a water glycerol solution [12]. At the small length scale probed by X-ray, the dependency of the surface tension on the scattering vector was evaluated and a debate with theoretical predictions is currently in progress [13–16].

In this work a surface light scattering study under total internal reflection at the air-aqueous media interfaces is presented. Three systems were investigated: pure water, a latex dispersion and an amphiphilic diblock copolymer solution. Due to its amphiphilic nature, the block copolymer occupies the interface and modifies its properties. The latex particles on the other hand hardly affect the interface, since they are not adsorbed [17]. A comparison of the two samples therefore allows a distinction between surface and bulk scattering effects.

2 Experiment

2.1 Surface light scattering

Recently we have described a new apparatus which implements a cylindrical scattering geometry, shown schematically in Figure 1 [18,19]. This geometry allows illumination and scattering detection for a liquid-liquid or a liquid-

air interface from any angle above or below the interface. The apparatus consists of a commercial goniometer (Optrel, Kleinmachnow, Germany) with two arms (laser arm and detector arm). The light source is a 25 mW HeNe-laser (wavelength $\lambda = 633$ nm) and the detector for scattering experiments is an avalanche photodiode. A cylindrical glass sample cell (diameter 7.5 cm, total volume 250 mL) was placed in the center of the goniometer, aligned to its axis of rotation. To avoid external distortions, the apparatus is placed on an active vibration damping table TS140 (HWL, Ammerbuch, Germany). The set-up combines evanescent wave dynamic light scattering (EWDLS) with ellipsometry. Its flexibility allows us to change the incident angle φ and detection angle ψ within the whole 360 degree range (see Fig. 1). The possibility for scattering measurements out of the reflection plane was not used in this work.

The access to the critical angle φ_0 is an important issue for scattering investigations at the surface [1]. For $\varphi > \varphi_0$, total reflection takes place and an evanescent wave is generated in medium 2 of the lower refractive index n_2 (air, in this case). The penetration depth of the generated evanescent wave is calculated from Snell's law:

$$n_1 \sin(\varphi) = n_2 \sin(\varphi'). \qquad (1)$$

Here, n_1 is the higher refractive index of medium 1 (water) at the illumination side and φ' is the angle of the refracted beam. The wave vector $k'_\perp$ component perpendicular to the interface of the refracted beam reads

$$k'_\perp = n_2 k_0 \cos(\varphi') = n_2 k_0 \sqrt{1 - \frac{n_1^2}{n_2^2} \sin^2 \varphi}, \qquad (2)$$

where $k_0 = 2\pi\lambda^{-1}$. The oscillation $\exp(ik'_\perp z)$ of the refracted beam for $\varphi < \varphi_0$ becomes an exponential decay $\exp(-|k'_\perp|z)$ for $\varphi > \varphi_0$, where equation (2) yields a complex value for $k'_\perp$. The penetration depth of the evanescent wave generated in this case is $d_p = |k'_\perp|^{-1}$. Using the evanescent wave as illumination for a scattering experiment, an intensity enhancement at φ_0 is predicted from Maxwell's theory [20]. For $\varphi = \varphi_0$ the amplitude of the evanescent wave amounts to twice the amplitude of incident field. This enhancement of the incident field translates to an enhancement of the scattered field and a scattered intensity amplification up to a factor of 4 is expected.

Static scattered intensity I_s was measured in a wide range $30 < \varphi$ (degrees) < 70 of the incident angle, keeping the scattered angle $\psi = 20°$ fixed. In a second experiment, the incidence angle was fixed at a value $\varphi = 35°$ below φ_0 and the scattered angle was scanned in the range $44 < \psi$ (degrees) < 52. For the static and dynamic scattering experiments, the light was always polarized in the direction parallel to the reflection plane (p-polarization). Intensity autocorrelation functions $g_2(q_\parallel, t)$ were measured varying the parallel component of the scattering vector

$$q_\parallel = n_1 k_0 [\sin(\varphi) - \sin(\psi)], \qquad (3)$$

in a relative small angular range ($56 < \psi$ (degrees) < 63). The incident angle $\varphi = 65°$ is chosen significantly above

the critical angle $\varphi_0 = \arcsin(1/n_{\mathrm{H_2O}}) \approx 48.6°$ of total internal reflection in order to have a high surface sensitivity, *i.e.* a small penetration depth $d_p \approx 150\,\mathrm{nm}$ of the evanescent wave. Since also $\psi > \varphi_0$, the geometry applied for EWDLS measurements is double evanescent.

It must be pointed out that throughout this work the measured scattering phenomena are related directly to the surface dynamics itself, rather than to the Brownian diffusion of colloids or polymers as probed by standard bulk light scattering technique [6].

2.2 Sample preparation

Double distilled and de-ionized water from a Milli-Q-RG ultrafiltration system was used with $10^{-7}\,\mathrm{wt\%}$ of $\mathrm{NaN_3}$, a bactericide agent. It was added to avoid the growth of microorganisms. The cylindrical cell was accurately cleaned in an ultrasound bath using a $4\,\mathrm{wt\%}$ Hellmanex (Hellma, Germany) solution and successively pure water, then the cell was rinsed using ethanol and eventually pure water. Half of the volume of the cylindrical cell was filled with a syringe. Using a pump connected to a long needle, it was possible to clean the interface from dust, impurities and bubbles trapped at the walls. This cleaning step was repeated several times.

$50\,\mu\mathrm{L}$ of the latex dispersion or the aqueous polymer solution (concentrations c between 0.03 and $1\,\mathrm{g\,L^{-1}}$) were placed with a micro-syringe (gastight Hamilton) on the top of the water surface. The overall concentration in the measuring cell was varied between 0.01 and $3\,\mathrm{mg\,L^{-1}}$.

The highly monodisperse poly(styrene) (PS) latex was prepared by emulsion polymerization in the presence of peroxidisulfate. The latter component ensured the ionic stability of the dispersion. The spherical latex has a hydrodynamic radius $R_h = 52.3\,\mathrm{nm}$ (measured by conventional dynamic light scattering). The polymer, a symmetric diblock copolymer composed of poly(isoprene) (PI) and poly(ethylene oxide) (PEO), was synthesized by anionic polymerization using high vacuum techniques [21, 22]. It has a molecular weight $M_w = 16400\,\mathrm{g/mol}$, a polydispersity $M_w/M_n = 1.03$, and the weight fraction of PI is 46%. The amount of the added dispersion or solution was small and did not change significantly the level of the interface and did not affect the alignment of the beam.

3 Experimental results

3.1 Surface static scattering

For surface static light scattering (S-SLS) experiments (*p*-polarization), I_s was measured as a function of the incident angle at a fixed scattered angle ($\psi = 20°$). A narrow and intense peak almost two orders of magnitude higher than the background and with a width around 0.3° was observed at φ_0 at the air-water interface, shown in Figure 2. The peak was observed in *s*-polarization as well, and could be also detected in a scan of the detector angle (inset of Fig. 2). The location of the peak directly at φ_0
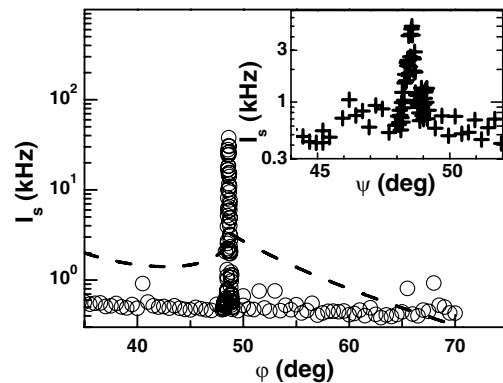
Fig. 2. Scattered intensity I_s in *p*-polarization as a function of the incident angle φ for a scattered angle $\psi = 20°$ at the bare air-water interface. The dashed line represents the typical shape of a Yoneda peak calculated by the diffuse reflection theory [24]. Inset: I_s as a function of the scattered angle ψ for an incident angle $\varphi = 35°$.

resembles the Yoneda peak in X-ray studies [23,24]. For a comparison, Figure 2 contains a calculated Yoneda peak profile based on the diffusive reflection theory (see Eq. (7) below) [24]. The latter theory, however, cannot account for the sharpness and relative height of the peak observed in this work.

The same result is found with a PS dispersion at two concentrations (0.01 and $0.1\,\mathrm{mg\,L^{-1}}$), as displayed in Figure 3a. The high and narrow peak becomes slightly sharper and higher with increasing latex concentration. On the other hand, the average background intensity away from the peak is not significantly affected. This background is only marginally above the detector dark signal (0.25 kHz). The same scans were performed over a wide range of concentration of the diblock copolymer PI-PEO. The sharp peak seen at low concentrations is displayed in Figure 3b (see also right inset). In this case, the presence of a surface active polymer, at intermediate and high concentration, broadens the observed peak which tends to disappear at the highest concentration studied. The background intensity significantly increases at the highest concentrations (see left inset in Fig. 3b). At low concentration, the scattering signal can be attributed to the surface fluctuations, whereas the significant increase of intensity at high concentration is likely due to bulk scattering.

Before concluding this section, let us evaluate the scattering from surface density fluctuations. The ratio between the scattered intensity $I_\parallel$ due to density fluctuations (corresponding to the horizontal displacement $\xi(r,t) = \xi_{q_\parallel}(t)e^{iq_\parallel r}$) and caused by amplitude fluctuation $I_\perp$ (corresponding to the vertical displacement $\zeta(r,t) = \zeta_{q_\parallel}(t)e^{iq_\parallel r}$) was calculated by Bouchiat and Langevin [25]:

$$\frac{I_\parallel}{I_\perp} \sim \frac{\gamma}{K}(q_\parallel d)^2, \tag{4}$$

where γ is the surface tension, K ($= \mathrm{d}\gamma/\mathrm{d}\ln A$; A is the area per molecule) is the surface compressibility modulus. Surface tension measurements on the block copolymer
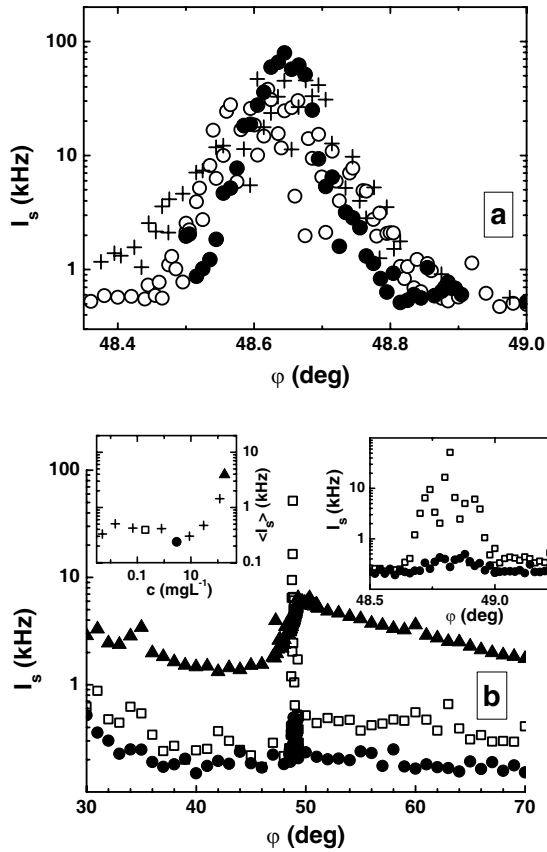
Fig. 3. a) Scattered intensity as a function of the incident angle φ around the critical angle: bare interface (+) and PS latex concentration $c = 0.01\,\mathrm{mg\,L^{-1}}$ (○) and $0.1\,\mathrm{mg\,L^{-1}}$ (●). b) Scattered intensity I_s as a function of the incident angle for polymer concentrations $0.2\,\mathrm{mg\,L^{-1}}$ (□); $3\,\mathrm{mg\,L^{-1}}$ (●); $180\,\mathrm{mg\,L^{-1}}$ (▲). Right inset: I_s measured around the critical angle for $c = 0.2\,\mathrm{mg\,L^{-1}}$ (□) and $3\,\mathrm{mg\,L^{-1}}$ (●). Left inset: plot of the average scattered intensity (+) *vs.* polymer concentration. The concentrations shown in the main plot and insets are marked by corresponding symbols.

3.2 Surface dynamic scattering

The capillary wave dynamics for all samples was investigated by EWDLS. At the lowest concentrations studied, no significant scattering from the bulk was observed. This

sample at a nominal concentration $c = 0.2\,\mathrm{mg\,L^{-1}}$ yielded $\gamma = 69\,\mathrm{mN\,m^{-1}}$ and $K \approx 10\,\mathrm{mN\,m^{-1}}$. The layer thickness $d = 8.6\,\mathrm{nm}$ is estimated by the sum of the sizes of the unperturbed PI coil in dodecane and the unperturbed PEO coil in water. These coil dimensions are estimated on the basis of the freely rotating model for the bonds in the polymer chain [26]. Plugging these numbers into equation (4) and considering a typical $q_{\parallel} = 0.5\,\mu\mathrm{m^{-1}}$, the intensity ratio becomes $I_{\parallel}/I_{\perp} \sim 10^{-4}$. Hence, the scattering contribution due to density fluctuations within the interface is not significant and the interface scattering can be safely attributed to the fluctuations in the vertical displacement.

allowed us to study surface dynamic scattering up to a limiting concentration, above which it was not possible to detect propagating waves anymore. Above this concentration limit, the scattering was dominated by bulk contribution.

The correlation functions presented here are related to the height-height correlation function due to the surface roughness. A mathematical description of the displacement of the interface from its equilibrium plane is given by $\zeta(x,t) = \zeta_0 \exp i(q_{\parallel}x + \omega^* t)$, for a wave vector $q_{\parallel}$ in x direction. The complex frequency $\omega^* \,(= \omega + i\Gamma)$ represents the evolution of the surface mode: it oscillates with a frequency ω and decays with a damping constant Γ [8]. The motion at the surface affects also the bulk of the fluid. The fluctuations due to capillary wave penetrate into the bulk with a decay length related to the wavelength of the surface $\sim q_{\parallel}^{-1}$. At small scattering vectors $q_{\parallel}$, the theoretical dispersion relations read [2]

$$\omega = (\gamma q_{\parallel}^3/\rho)^{1/2}, \tag{5a}$$

$$\Gamma = 2\eta q_{\parallel}^2/\rho, \tag{5b}$$

where ρ and η denote the density and the dynamic viscosity.

These fluctuations can be detected by dynamic light scattering, where the intensity correlation function depends on ω and Γ. The fitting function used in the analysis was introduced by Gutt *et al.* [7].

$$g_2(q_{\parallel},t) - 1 = \frac{\langle I(q_{\parallel},t')I(q_{\parallel},t'+t)\rangle_{t'}}{\langle I(q_{\parallel},t')^2\rangle_{t'}} - 1$$
$$\sim 2I_s I_r \cos(\omega t)\exp(-\Gamma t) + I_s^2 \exp(-2\Gamma t). \tag{6}$$

As in the case of XPCS, heterodyne mixing was observed in our experiments. Because of the analogy with the evanescent illumination scheme, we preferred to use this latter correlation function although other fitting functions were used in SQELS accounting for heterodyne signals [8]. Additionally, the parameter ϕ (accounting for the deviation of the real spectrum from a Lorentzian form) and β (accounting for the instrumental broadening) entering in the SQELS fitting functions can be correlated to ω and Γ [9] and mislead the physical interpretation of the results. The origin of the heterodyne signal remains unclear to us. As it is suggested for X-ray, it can be related to a coherent interference between the scattering and the total reflected electric field [7].

The intensity autocorrelation functions $g_2(q_{\parallel},t)$ at the bare air-water interface are displayed in Figure 4a. At high $q_{\parallel}$ the oscillations were not detectable in the time window of EWDLS experiments. With equation (6), it was possible to fit the correlation functions in the time and scattering vector range where the surface fluctuations were detectable. I_s, I_r, ω and Γ could be fitted together. The first two quantities are related to the amplitude of the oscillation, whereas the last two describe the complex frequency of the capillary wave.
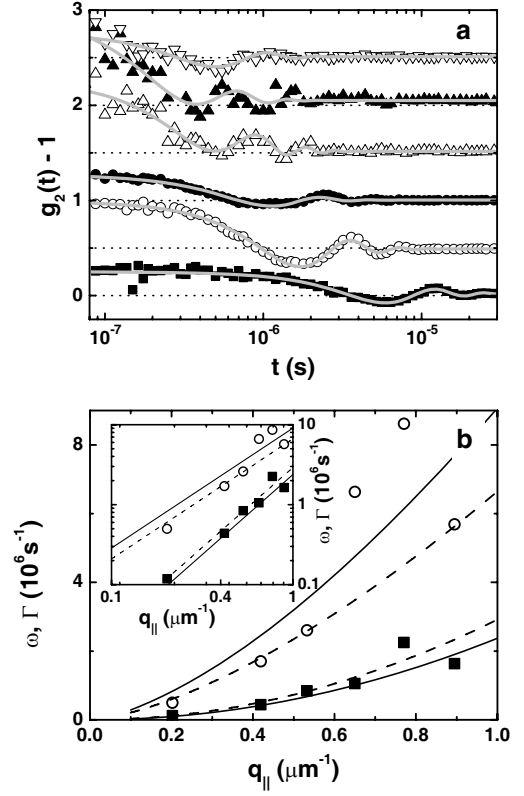
The results of the fits for ω and Γ are shown in Figure 4b. The predicted scaling (5a) and (5b) for small scattering vectors was imposed to extract the surface tension
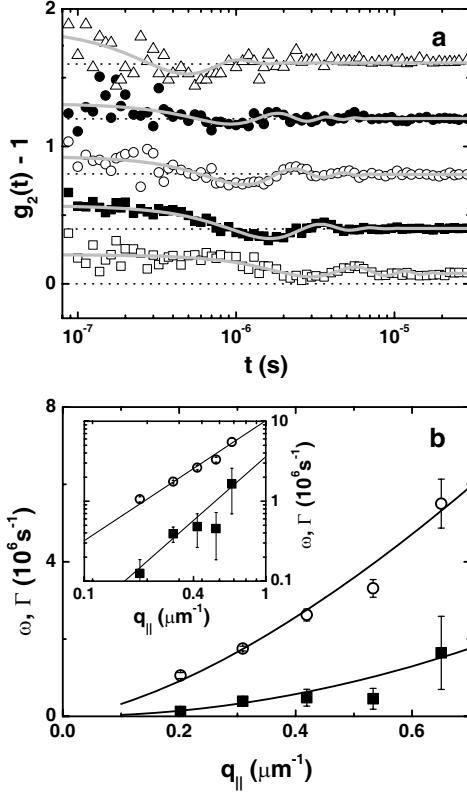
Fig. 4. a) Intensity autocorrelation functions at the bare air-water interface for different $q_\parallel$: 0.20, 0.30, 0.41, 0.53, 0.65 μm^{-1} (from the bottom to the top). For better visibility the curves are shifted in steps of 0.4 units on the y-axis and for the lowest $q_\parallel$ (0.20 μm^{-1}) $g_2(t) - 1$ is magnified by a factor of 10. b) Experimentally determined dispersion relation of the propagation frequency ω (○) and damping constant Γ (■) at the bare air-water interface. The solid lines are fits of equations (5a) and (5b). Inset: double-logarithmic representation of the data.

Fig. 5. a) Intensity autocorrelation functions at the PS latex bulk concentration $c = 0.01$ mg L^{-1} for different $q_\parallel$: 0.20, 0.41, 0.53, 0.65, 0.77, 0.89 μm^{-1} (from the bottom to the top). For better visibility the curves are shifted in steps of 0.5 units on the y-axis and for the lowest $q_\parallel$ (0.20 μm^{-1}) $g_2(t) - 1$ is magnified by a factor 4. b) Experimentally determined dispersion relation of the propagation frequency ω (○) and damping constant Γ (■) at the PS latex bulk concentration $c = 0.01$ mg L^{-1}. The solid lines are fits of equations (5a) and (5b). The dashed lines do not consider the points at $q_\parallel = 0.65$ μm^{-1} and $q_\parallel = 0.77$ μm^{-1}. Inset: double-logarithmic representation of the data.

and the viscosity. Despite the large error bars of ω and Γ at the highest scattering vectors, the measurements were quite accurate. Furthermore, it is found that the experimental dispersion relations follow the theoretical scaling.

The same experiments were carried out for the dispersion of 0.01 mg L^{-1} of PS latex. Autocorrelation functions were detected in a similar scattering vector range (see Fig. 5a) and despite the deviation of the values at $q_\parallel = 0.65$ μm^{-1} and $q_\parallel = 0.77$ μm^{-1} also in this case the experimental dispersion relations follow the theoretical scaling (see Fig. 5b). The error bars in this last case are much smaller than for bare water surface. The values of the slopes of ω and Γ are reported in Table 1, and these results will be discussed together with the others in the following section. When increasing the concentration of PS particles by one order of magnitude, it was not possible to detect properly propagating capillary waves. The autocorrelation functions become flat in the time region where the propagation was observed, whereas a decay was detected at larger time compatible with the relaxation due to bulk diffusion $\tau = D^{-1}q^{-2}$ (where D is the diffusion coefficient). The number of PS particles was also high
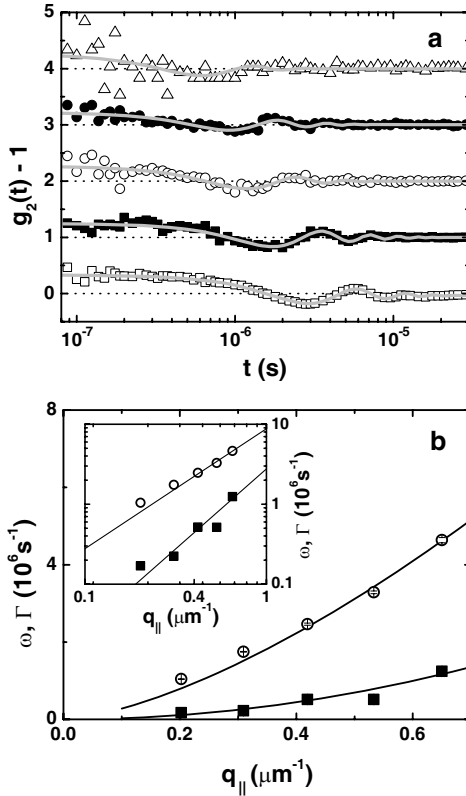
enough to detect autocorrelations at high scattering vectors, where Brownian diffusion of the particles is typically observed. Thus, despite the fact that the time scale of capillary wave's propagation and Brownian diffusion differ by several orders of magnitude, the Brownian diffusion can mask the dynamics due to the surface roughness.

The last series of data deals with the interfacial behavior of PI-PEO. In Figures 6 and 7, the analysis on the intensity autocorrelation functions are displayed at the polymer concentrations $c = 0.015$ mg L^{-1} and 0.2 mg L^{-1}, respectively. The autocorrelation functions relative to the first concentration shown are observed in the same range as the ones at the bare air-water interface. In this case, the accuracy of the fit is also good (see Fig. 6b), with a good agreement with the theoretical scaling (Eqs. (5a) and (5b)). At the diblock copolymer concentration 0.2 mg L^{-1}, the autocorrelation functions clearly evidence a propagation of capillary waves up to $q_\parallel = 0.89$ μm^{-1} (see Fig. 7a). It is also worth noticing

Table 1. Dispersion of the frequency ω and damping constant Γ for all investigated systems obtained from fits of equations (5a) and (5b). The last two columns show the calculated values of the surface tension and viscosity upon the hypothesis of a constant density $\rho = 998.2\,\mathrm{kg\,m^3}$. The data for the row PS* are obtained from the dashed line of Figure 5b.
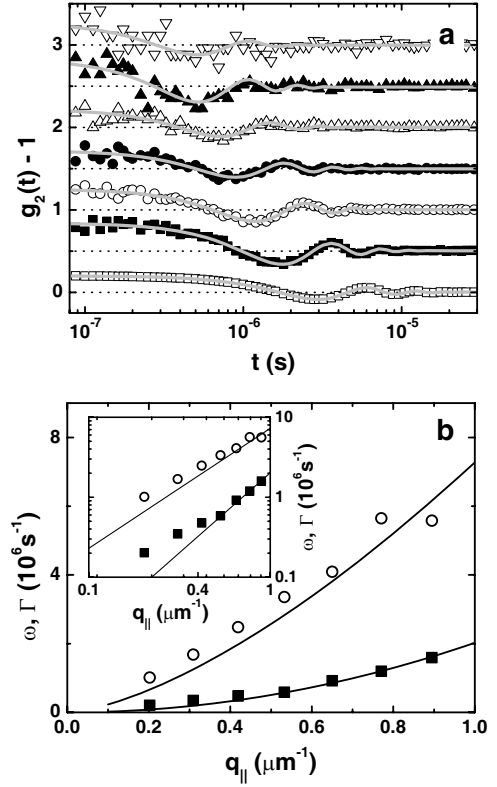
System	$c\ (\mathrm{mg\,L^{-1}})$	$\dfrac{\omega}{q_\parallel^{3/2}}\ (10^6\,\frac{\mathrm{s^{-1}}}{\mu\mathrm{m}^{-3/2}})$	$\dfrac{\Gamma}{q_\parallel^2}\ (10^6\,\frac{\mathrm{s^{-1}}}{\mu\mathrm{m}^{-2}})$	$\gamma\ (\mathrm{mN\,m^{-1}})$	$\eta\ (10^{-3}\mathrm{Pa\,s})$
water	–	10.0	3.6	102	1.80
PS	0.01	9.1	2.3	82	1.19
PS*	0.01	6.7	2.9	44	1.46
PI-PEO	0.015	8.8	2.8	77	1.38
PI-PEO	0.068	7.3	1.8	53	0.91
PI-PEO	0.2	7.3	2.0	52	1.00

Fig. 6. a) Intensity autocorrelation functions at the polymer bulk concentration $c = 0.015\,\mathrm{mg\,L^{-1}}$ for different $q_\parallel$: 0.20, 0.31, 0.41, 0.53, 0.65 $\mu\mathrm{m}^{-1}$ (from the bottom to the top). For better visibility the curves are shifted in steps of 1 unit along the y-axis and for the lowest $q_\parallel$ ($0.20\,\mu\mathrm{m}^{-1}$) $g_2(t) - 1$ is magnified by a factor 10. b) Experimentally determined dispersion relation of the propagation frequency ω ($\circ$) and damping constant Γ ($\blacksquare$) at the polymer bulk concentration $c = 0.015\,\mathrm{mg\,L^{-1}}$. The solid lines are fits of equations (5a) and (5b). Inset: double-logarithmic representation of the data.

Fig. 7. a) Intensity autocorrelation functions at the polymer bulk concentration $c = 0.2\,\mathrm{mg\,L^{-1}}$ for different $q_\parallel$: 0.20, 0.31, 0.41, 0.53, 0.65, 0.77, 0.89 $\mu\mathrm{m}^{-1}$ (from the bottom to the top). For better visibility the curves are shifted in steps of 1 unit along the y-axis. b) Experimentally determined dispersion relation of the propagation frequency ω ($\circ$) and damping constant Γ ($\blacksquare$) at the polymer bulk concentration $c = 0.2\,\mathrm{mg\,L^{-1}}$. The solid lines are fits of equations (5a) and (5b). Inset: double-logarithmic representation of the data.

that when imposing the theoretical scaling of the dispersion relations in the small-$q_\parallel$ approximation (Eqs. (5a) and (5b)), ω and Γ show significant deviations at small scattering vectors. The results, including an intermediate concentration, are summarized in Table 1.

Comparing all our dynamic results with the recent literature [7], it can be noticed that due to the detec-

tion through a single mode fiber, the signal-to-noise ratio is much better than in XPCS. Despite the fact that the range of scattering vectors $q_\parallel$ accessible by XPCS is wider than for EWDLS [27], the highest $q_\parallel$ at which capillary waves were detected at a liquid surface by XPCS was $q_{\parallel,\mathrm{max}} = 700\,\mathrm{cm^{-1}} = 0.07\,\mu\mathrm{m}^{-1}$. In the experiments presented here, it was possible to detect a propagating capillary wave for $q_{\parallel,\mathrm{max}} = 0.89\,\mu\mathrm{m}^{-1}$, more than one or-

der of magnitude larger than in XPCS measurements [7]. In addition, the present study shows that by light scattering also capillary waves on low viscosity fluids with water as the most important example can be accessed. XPCS studies so far were restricted to high-viscosity samples with slow dynamics. The advantage in light scattering is the high flux of coherent photons provided by a laser. To resolve a dynamical process, sufficient photons per relaxation time or per inverse oscillation frequency are required.

3.3 Summary of the experimental results

At low concentrations, surface static light scattering measurements revealed the presence of a high and narrow peak (see Figs. 2 and 3). When adding PI-PEO diblock copolymer at the bare water surface, the peak becomes smaller and at $c = 3\,\mathrm{mg\,L^{-1}}$ it almost disappears. Above this last concentration, the main contribution to the scattering can be attributed to bulk scattering. In the case of the dispersions of PS latex, the main contribution of the scattered intensity, in the concentration range studied, can be ascribed only to the surface scattering (see Fig. 3).

In the same range of concentrations where the sharp peak was observed, propagation of capillary waves was detected under total reflection. To the best of our knowledge, it is the first time that correlation functions describing propagating capillary waves could be measured (see Figs. 4a, 5a, 6a and 7a) in a range of large scattering vector $q_\parallel$ which was up to now not accessible to SQELS and not yet measured by XPCS. The observed surface modes can be described by the height-height correlation function [7]. The autocorrelation functions $g_2(q_\parallel, t)$ can be fitted according to equation (6) and the predicted scaling dispersion relations (Eqs. (5a) and (5b)) can be applied in the system considered (see Figs. 4, 5, 6 and 7).

In Table 1, the fits of the experimental dispersion relations (see Figs. 4b, 5b, 6b and 7b) are shown together with the calculated surface tension and viscosity. For the calculation of these quantities the density is considered constant and equal to the water bulk value. $\frac{\omega}{q_\parallel^{3/2}}$ decreases from $10.0 \times 10^6\,\mathrm{s^{-1}\,\mu m^{3/2}}$ for the bare air-water interface to $7.3 \times 10^6\,\mathrm{s^{-1}\,\mu m^{3/2}}$, in the case of a copolymer concentration $c = 0.2\,\mathrm{mg\,L^{-1}}$. This latter decreasing value could be related to the change of the surface tension, but the lowering cannot be simply quantified by the dispersion relation $\gamma = (\omega q_\parallel^{-3/2})^2 \rho$, as one can see in the variation of the γ values in Table 1. The values of the viscosity calculated from the relation $\eta = \Gamma q_\parallel^{-2} \rho / 2$ also decrease when the concentration is increased (see last column in Tab. 1).

4 Discussion

4.1 Scattering peak at the critical angle

Several techniques were applied to resolve the interfacial profiles and to quantify the surface roughness [28]. A well-known feature of the diffuse X-ray scattering is the Yoneda peak [23,24]. This peak is predicted when the incident or the scattered angle approaches the critical angle. The amplitude I_Y depends on the refractive index of the media and on the scattering vector.

In the work presented here, from surface static light scattering experiments it was observed that the scattered intensity increases dramatically when the incident angle φ, or the scattered angle ψ, approaches the critical angle (see Figs. 2 and 3). This phenomenon was observed at low concentration for all the systems studied at the air-water interface.

The scattering diffuse cross-section due to the roughness of the liquid surface [23–25], in the distorted-wave Born approximation, reads [24]

$$\left| \frac{\mathrm{d}\sigma}{\mathrm{d}\Omega} \right|_{\mathrm{diff}} = (L_x L_y) \frac{|k_0^2(1 - n^2)|^2}{16\pi^2} |T(k_1)|^2 |T(k_2)|^2 S(q_\parallel),$$

$$(7)$$

where $L_x L_y$ is the illuminated area, n is the refractive index, $T(k_1)$ and $T(k_2)$ are the Fresnel transmission coefficients for the incident and scattered wave vector and for very small scattering vectors $S(q_\parallel)$ is related to the Fourier transform of the height-height correlation function of the surface. The origin of the Yoneda scattering is related to the behavior of the functions $T(k_1)$ and $T(k_2)$ in equation (7) at the critical angle. The latter equation is symmetric with respect to the incident and scattered wave vector, however the maximum in diffusive intensity at the critical angle can differ for the incident and scattered vector because of the different illuminated area [24].

The data shown in Figure 2 display reciprocity for k_1 and k_2 as the Yoneda peak. However, even if the phenomenology observed is similar to the one of the Yoneda wings, diffuse scattering theory cannot provide a quantitative interpretation for our experimental findings.

In physical terms, a simple understanding of the sharp peak is achieved as follows. A capillary wave leads to a periodic modulation of the local amplitude reflection coefficient $r_v(\mathbf{r})$ ($v \in \{p, s\}$) in p-polarization or s-polarization, because the modulation of the local surface normal leads to a modulation $\Delta\varphi(\mathbf{r})$ of the angle of incidence. The amplitude of the resulting light scattering is proportional to the amplitude of the capillary wave and a contrast factor $\mathrm{d}r_v/\mathrm{d}\varphi$. This first-order effect in $\Delta\varphi(\mathbf{r})$ is expected to reproduce the broad and weak Yoneda peak described by classical theory with weak contrast variation. At the critical angle, there is additionally another type of scattering contrast. At spots with $\Delta\varphi(\mathbf{r}) < 0$, *i.e.* where the local angle of incidence $\varphi_0 + \Delta\varphi(\mathbf{r})$ is smaller than φ_0, the light passes the interface as a refracted beam. For spots with $\Delta\varphi(\mathbf{r}) > 0$, in contrast, the condition of total internal reflection is fulfilled. In a simplistic view, an evanescent wave is formed for those spots instead of the refracted beam. The described scattering contrast contributes only close to the critical angle, where the small variation $\Delta\varphi(\mathbf{r})$ switches the local conditions from transmission to total reflection. This behavior corresponds to our observation of a narrow peak.

The discussion so far is based on the simplified description of a total internal reflection geometry, where the

sharply defined angle of incidence corresponds to a singular wave vector direction of the incident beam. Such a well defined wave vector is present only for a plane wave with infinite width. In a real experiment with finite beam width w, in contrast, there is unavoidably a distribution of wave vector directions, *e.g.* due to weak focusing of a beam. The width $\delta\varphi$ of this distribution determines the angular range where the second contrast mechanism is operational and therefore it determines the angular width of the sharp peak. In our experiments, a cylindrical lens of focal length $f = 150\,\mathrm{mm}$ is used for a weak focusing of the beam on the surface. With $w \approx 0.5\,\mathrm{mm}$ at the lens, the angular smearing and therefore the peak width is estimated as $\delta\varphi \approx w/f = 0.2°$. This value fits well to the experimental observation (see Fig. 3). The local slope of the interface within a capillary wave yields a second contribution of smearing $\delta\varphi_c$, which however is two orders of magnitude lower than $\delta\varphi$ and therefore can be neglected. The estimate $\delta\varphi_c = \langle\zeta^2\rangle^{1/2}/(2\pi/q)$ is based on the mean square amplitude $\langle\zeta^2\rangle = k_\mathrm{B}T/(2\pi\gamma)\ln(l_c * q)$ of interfacial fluctuations with wave vectors in the range $0 \ldots q$, where $k_\mathrm{B}T$ is the thermal energy and $l_c \approx 2\,\mathrm{mm}$ is the capillary length [1].

The distribution of incident wave vector directions is of further relevance to solve an apparent contradiction. When approaching φ_0 from small φ, the angle of refraction φ' approaches $90°$, *i.e.* a propagation parallel to the interface with no perpendicular penetration into the low refractive index medium. When approaching φ_0 from large φ on the other hand, the penetration depth of the evanescent wave increases, with a divergence, *i.e.* infinite penetration at $\varphi = \varphi_0$. Both arguments rely on a sharply defined wave vector of the incident beam. The apparent contradiction is resolved for a beam of finite width w and finite divergence, where the transition from the refracted beam to an evanescent wave is smoothened and w enters as an additional length scale. Smoothing effects are expected as soon as the width of the refracted beam $w\cos(\varphi')/\cos(\varphi)$ becomes comparable to λ. A similar smoothing effect is discussed for ellipsometry measurements at the critical angle [29,30]. Clearly, a realistic description of an evanescent wave geometry has to take the finite beam width and the corresponding distribution of wave vector directions into account.

A more formal understanding of the narrow peak at φ_0 is based on the shape of r_v. For a sharp transition of refractive index at an interface, r_v is real for $\varphi < \varphi_0$ and complex for $\varphi > \varphi_0$. The transition results in a step of the slope $\mathrm{d}r_v/\mathrm{d}\varphi$, also visible as a step of the slope of the intensity reflectivity $|r_v|^2$. The step in slope implies a δ-function $\delta(\varphi - \varphi_0)$ in the second derivative $\mathrm{d}^2r_v/\mathrm{d}\varphi^2$. This δ-function folded with the distribution of directions of the incident wave vector is assumed to reproduce the observed narrow peak. The occurrence of the second derivative indicates an effect of second order. The high order might explain why the effect was overlooked so far. At φ_0 —the *critical* angle— the enhancement appears to outweigh the weakness of a second-order perturbation. Additionally the second-order term allows a mixing of two capillary waves with wave vectors $\mathbf{q}_\parallel^{(1)}$ and $\mathbf{q}_\parallel^{(2)}$, the sum of which amounts

to the wave vector $\mathbf{q}_\parallel$ realized in the experiment. Thus, more than a single excitation can contribute to the scattering. Meunier discusses reflectivity of liquid interfaces and concludes that the effect of second-order scattering is weak for X-rays due to the tiny refractive index contrast for this radiation [31]. Therefore it is not surprising that a similar effect was not yet observed in X-ray scattering. Although his main focus is on the Brewster angle, Meunier mentions already that the neglection of different local slopes becomes only a rough approximation close to the critical angle. A further quantity of interest is the steepness $\mathrm{d}n/\mathrm{d}z$ of the refractive index profile $n(z)$. Only in an idealized picture $n(z)$ is a step function, whereas actually the profile is steady, but possibly quite steep. For a monotonous $n(z)$, $|\mathrm{d}n/\mathrm{d}z|$ has the shape of a peak. With preset φ, the angle $\varphi'(z)$ of the local wave vector at depth z is calculated from Snell's law 1 by inserting $n_2 = n(z)$. As a consequence, $\varphi'(z)$ depends on the local refractive index $n(z)$, but not on the general shape of the profile. Close to φ_0 the condition $\varphi'(z) = 0$ of total internal reflection at depth z is directly connected to a specific value of φ. Thus, the described intensity enhancement operates mainly at a well-defined depth, selected by the actual angle φ. The $|\mathrm{d}n/\mathrm{d}z|$ peak therefore induces a peak in the φ-dependent amplification $A(\varphi)$. The narrow peak observed in the experiment involves a convolution with the $A(\varphi)$ peak. With this mechanism, the steepness of the refractive index profile directly affects the height and width of the narrow peak at φ_0. When the profile becomes less steep, the $|\mathrm{d}n/\mathrm{d}z|$ peak becomes smaller and wider, inducing a weakening and broadening of the $A(\varphi)$ peak and therefore the scattering peak observed in the experiment. A related effect is the enhanced scattering of an evanescent wave in a smooth and more extended refractive index profile [32]. The smoother profile for the liquid crystalline sample investigated in that work leads to a wider $A(\varphi)$ peak and therefore a less high signal distributed over a wider φ-range. Due to birefringence effects, the refractive index profile is different for s and p polarization and the enhancement was observed only for p-polarization. Simple qualitative simulations [33] lead to the interpretation discussed in this work.

A critical concentration of the diblock copolymer was found, above which the peak cannot be observed anymore. The disappearance of the sharp peak with increasing concentration (see Fig. 2) might be attributed to a partial masking by bulk scattering contributions. A detailed comparison shows, however, that the background at the highest polymer concentration does not reach the former magnitude of the peak without added polymer (see Fig. 3). The disappearance of the peak thus is not purely due to masking by bulk scattering. Rather, the polymer smoothens the interfacial refractive index profile and therefore affects $\mathrm{d}n/\mathrm{d}z$ and $A(\varphi)$, which in turn has an effect on the scattering enhancement at the peak. For the latex particles, on the other hand, the peak does not disappear, even at the highest concentration. Since the PS latexes do not adsorb to the interface and hardly affect $\mathrm{d}n/\mathrm{d}z$, the presence of the peak over the whole concentration range fits the interpretation.

4.2 Capillary waves

The time evolution of the capillary wave phenomenon is for the first time studied by EWDLS. It is shown that this new method leads to significant improvements, comparing to SQELS and XPCS, in the autocorrelation function time range and the $q_\parallel$-space resolution.

In this work equation (6) was used to fit the intensity autocorrelation functions. In fact, in the phenomenological approach applied to SQELS [8] a large number of parameters must be fitted. Although the surface viscoelastic moduli can be extracted from the analysis of the spectrum $P(\omega)$ or of the correlation function, Cicuta [9] has shown that reliable fits can be obtained only for a limited range of viscoelastic moduli [10]: for large value of dilatational modulus ϵ' (*e.g.* at high polymer interface concentration) no fitting procedure is stable.

Here, the surface tension and the viscosity were calculated using the approximated dispersion relations from the values of the propagating frequency ω and the damping constant Γ (see Tab. 1). Two strong hypothesis were made: a) the validity of the small $q_\parallel$ approximation for the dispersion relations (Eqs. (5a) and (5b)) and b) the surface tension and the viscosity are not $q_\parallel$-dependent. Within these approximations, an improvement, in particular of the Γ evaluation, comparing to the large overestimated values obtained by XPCS [7], was shown. Nonetheless, the outcomes of the surface tensions and viscosities seem to be either overestimated (at low concentrations) or underestimated (at high concentrations).
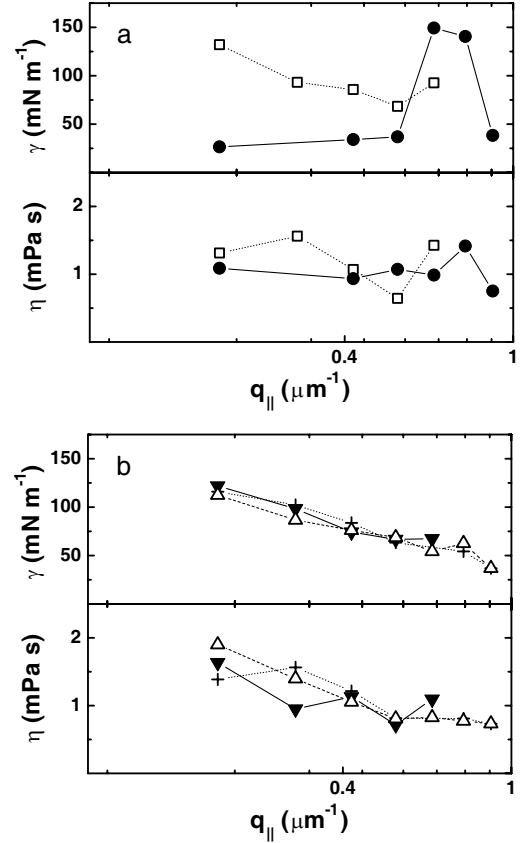
A different approach to discuss the result obtained is displayed in Figure 8. We remove the hypothesis of the $q_\parallel$-independent surface tension and viscosity. For the free surface of water and for other liquids, Langevin calculated corrections for the low $q_\parallel$ dispersion relations (Eqs. (5a) and (5b)) [1]

$$\omega = \sqrt{\frac{\gamma q_\parallel^3}{\rho}\left(1 - \frac{1}{2y^{3/4}}\right)}, \tag{8a}$$

$$\Gamma = \frac{2\eta q_\parallel^2}{\rho}\left(1 - \frac{1}{2y^{1/4}}\right), \tag{8b}$$

where $y = \gamma\rho/4\eta^2 q_\parallel$. The inversion of equations (8a) and (8b) was performed numerically, keeping the density constant, *i.e.* the bulk water value ($\rho_{\text{H}_2\text{O}} = 0.998\,\text{g/cm}^3$ [34]). Compared to an evaluation with the simple dispersion relations (Eqs. (5a) and (5b)), the results are lower by 2–15% for γ and 12–25% for η. The correction in equations (8a) and (8b) has a non-negligible effect in the available $q_\parallel$-range. Figure 8 shows the results. In most cases, γ is still overestimated in the low $q_\parallel$ region and underestimated at high $q_\parallel$. The results for η agrees reasonably well with the bulk viscosity $\eta_{\text{H}_2\text{O}} = 1.0\,\text{mPa s}$ of water [34].

There are several effects discussed in the literature which affect the detection of capillary waves and therefore can possibly influence the results. The value of Γ and therefore the resulting η are known to be sensitive on a smearing Δq of the q resolution [1,16]. A superposition of slightly different oscillation frequencies of varying q mimics a stronger decay because of dephasing with increasing t. Within the investigated angular range, the weak focusing of the laser and the detection by a single mode fiber provide low q smearing for a reasonable detection of Γ and η. Of more relevance are experimental effects on ω in order to understand the rather high results for γ. Gutt *et al.* discuss oscillations in $g_2(t)$ due to the creation or annihilation of two counterpropagating capillary waves [35]. These oscillations are predicted with double the frequency of the $g_1(t)$ oscillations. A wrong interpretation of an experimental oscillation frequency could possibly lead to a wrong result for γ. However, experimental data allow a distinction between heterodyne $g_1(t)$ detection and homodyne $g_2(t)$ measurement. While $g_1(t)$ oscillations ($\sim \cos(\omega t)\exp(-\Gamma t)$) are centered around the correlation baseline, $g_2(t)$ oscillations ($\sim \cos^2(\omega t)\exp(-2\Gamma t)$) occur above the baseline [16]. The data in Figures 4–7 clearly show a heterodyne signature, as assumed in the data evaluation. Recently, another experimental effect on γ measurements based on capillary waves was discussed for the case that in the calculation of scattering power the lateral motion within a capillary wave cannot be neglected compared to the movement perpendicular to the interface [36]. Such an effect is expected if

Fig. 8. a) Surface tension γ and viscosity η as functions of the scattering angle $q_\parallel$ at the bare air-water interface ($\square$) and at $c(\text{PS}) = 0.01\,\text{mg L}^{-1}$ ($\bullet$). b) Surface tension and viscosity as functions of the scattering angle $q_\parallel$ at the diblock copolymer concentration $c = 0.015$ ($\blacktriangledown$), 0.068 ($+$), 0.2 ($\triangle$) mg L^{-1}.

the wave vector component perpendicular to the interface $q_\parallel$ is larger than $q_\perp$. Since in our experiment $q_\perp/q_\parallel > 12$, an effect of this type is not expected.

A further attempt to understand the high γ values could be based on a q-dependent interface tension. Starting from the issue to separate the effects of interfacial density profile and capillary waves, Mecke and Dietrich [14] predicted theoretically first a decrease followed by an increase of γ with q. Although this effect based on van der Waals interactions predominantly affects a length scale where q^{-1} becomes comparable to the molecular dimension or the width of the interfacial profile, a first decrease shows up already for smaller q-values. Since, however, we observe an increased γ, the effect based on short-ranged van der Waals interactions can be ruled out. Not included in the theory of Mecke and Dietrich are interactions of longer range, *e.g.* charge-charge interactions. The water interface is known to be negatively charged (see *e.g.* [37]). The interface charges could lead to an effective suppression of capillary waves, which would lead to an effective increase of γ at high $q_\parallel$. For the time being we cannot tell if this speculation is the reason for the high γ values detected in this work. The assumption can be cross-checked by a comparison with measurements on a non-polar liquids. Further, an extension of the $q_\parallel$ range to lower and (with additional heterodyning) higher values can provide a wider overview on the behavior of γ. Such extended investigations will be the subject of future work.

4.3 Comparison

From different viewpoints, two models can describe the surface roughness at fluid interfaces [3,4,28]. The first considers the interface profile as a continuous function that varies between the two bulk values, and it gives a "static" description where the thickness L of the interfacial region is related to the bulk correlation length ξ_b. In contrast, the second model is based on thermal excitation of capillary waves and it represents the "dynamic" evolution of the surface fluctuations. In the capillary wave theory, the square of the interfacial thickness L_{CW} is given by [1]

$$L_{CW}^2 = \frac{1}{2\pi} \int_{-\infty}^{+\infty} \frac{kT}{\gamma q_\parallel^2 + g\Delta\rho} \mathrm{d}q_x \mathrm{d}q_y, \qquad (9)$$

where $\Delta\rho$ is the density difference $\rho_1 - \rho_2$ between the two phases and q_x, q_y are the scattering vector components within the interfacial plane.

The two experiments reported here reflect these different viewpoints. While the narrow peak monitors the interfacial profile and its fluctuations, the capillary wave dynamics represents the dynamics of the interfacial roughness. The two experiments therefore represent complementary features of the interface. An illustration of these complementary approaches is seen with the PS latex sample. While there is hardly an effect of this sample on the peak shape, the bulk scattering of the latex particles masks the dynamics detected at a different angular range.

5 Conclusion

In a surface light scattering experiment with illumination through the water side a sharp peak is observed when the angle of incidence passes the critical angle of total internal reflection. The peak is discussed as a second-order effect in interfacial fluctuations, the scattering of which is strongly enhanced at the critical angle. Width and height of the peak are affected by the smearing of incidence directions of the illuminating light and the angular range for which the condition of total internal reflection is achieved locally within the refractive index profile. While a surface active block copolymer modifies the interfacial refractive index profile and thereby reduces the peak below the background bulk scattering, a PS latex sample with no adsorption to the interface hardly affects the peak shape.

In a complementary experiment, the time evolution of capillary waves on water was studied by evanescent wave dynamic light scattering. It was possible to measure the propagation of capillary wave up to a scattering vector $q_\parallel = 0.89\,\mu\mathrm{m}^{-1}$. Within the experimentally accessible concentration window for the block copolymer and the latex sample, only a small modification of interfacial dynamics was found.

A forthcoming paper will deal with the diffusion dynamics and the structure of the samples at higher concentrations.

References

1. D. Langevin, *Light Scattering by Liquid Surfaces and Complementary Techniques* (Marcel Dekker, New York, 1992).
2. H. Lamb, *Hydrodynamics* (Dover, New York, 1945).
3. D. Beaglehole, Phys. Rev. Lett. **58**, 1434 (1987).
4. J. Meunier, J. Phys. (Paris) **48**, 1819 (1987).
5. J.P.R. Day, C.D. Bain, Phys. Rev. E **76**, 041601 (2007).
6. B.J. Berne, R. Pecora, *Dynamic Light Scattering* (Dover Publications, Mineola, 2000).
7. C. Gutt, T. Ghaderi, V. Chamard, A. Madsen, T. Seydel, M. Tolan, M. Sprung, G. Grubel, S.K. Sinha, Phys. Rev. Lett. **91**, 61041 (2003).
8. J.C. Earnshaw, Adv. Colloid Interface Sci. **68**, 1 (1996).
9. P. Cicuta, I. Hopkinson, Colloid Surf. A **233**, 97 (2004).
10. D.M.A. Buzza, Langmuir **18**, 8418 (2002).
11. S. Mora, J. Daillant, Eur. Phys. J. B **27**, 417 (2002).
12. A. Madsen, T. Seydel, M. Sprung, C. Gutt, M. Tolan, G. Grubel, Phys. Rev. Lett. **92**, 096104 (2004).
13. S. Mora, J. Daillant, K. Mecke, D. Luzet, A. Braslau, M. Alba, B. Struth, Phys. Rev. Lett. **90**, 216101 (2003).
14. K.R. Mecke, S. Dietrich, Phys. Rev. E **59**, 6766 (1999).
15. P. Tarazona, R. Checa, E. Chacon, Phys. Rev. Lett. **99** 196101 (2007).
16. C. Gutt, T. Ghaderi, M. Tolan, S.K. Sinha, G. Grübel, Phys. Rev. B **77**, 094133 (2008).

17. S.L. Kettlewell, A. Schmid, S. Fujii, D. Dupin, S.P. Armes, Langmuir **23**, 11381 (2007).
18. A. Stocco, PhD Thesis, University of Potsdam, Germany, 2007.
19. A. Stocco, G. Haseloff, A. Erbe, K. Tauer, R. Sigel, submitted to Phys. Rev. E.
20. W. Knoll, Annu. Rev. Phys. Chem. **49**, 569 (1998).
21. S. Pispas, N. Hadjichristidis, Langmuir **19**, 48 (2003).
22. S. Pispas, J. Polym. Sci. Part A: Polym. Chem. **44**, 606 (2006).
23. Y. Yoneda, Phys. Rev. **131**, 2010 (1963).
24. S.K. Sinha, E.B. Sirota, S. Garoff, H.B. Stanley, Phys. Rev. B **38**, 2297 (1988).
25. M.A. Bouchiat, D. Langevin, J. Colloid Interface Sci. **63**, 193 (1978).
26. M. Kurata, Y. Tsunashima, in *Polymer Handbook*, edited by J. Brandrup, E.H. Immergut, E.A. Grulke, 4th edition (Wiley, Hoboken, 1999) pp. VII/1-VII/83.
27. T. Thurn-Albrecht, W. Steffen, A. Patkowski, G. Meier, E.W. Fischer, G. Grubel, D.L. Abernathy, Phys. Rev. Lett. **77**, 5437 (1996).
28. D. Beysens, M. Robert, J. Chem. Phys. **87**, 3056 (1987).
29. G.E. Yakubov, B. Loppinet, H. Zhang, J. Rühe, R. Sigel, G. Fytas, Phys. Rev. Lett. **92**, 115501 (2004).
30. R. Sigel, A. Erbe, Appl. Opt. **47**, 2161 (2008).
31. J. Meunier, chapter 17 in *Light Scattering by Liquid Surfaces and Complementary Techniques*, edited by D. Langevin (Marcel Dekker, New York, 1992).
32. R. Sigel, G. Strobl, J. Chem. Phys. **112**, 1029 (2000).
33. R. Sigel, PhD Thesis, University of Freiburg, Germany, 1998.
34. D.R. Bloch, in *Polymer Handbook*, edited by J. Brandrup, E.H. Immergut, E.A. Grulke, 4th edition (Wiley, New Jersey, 1999) pp. III/59-61.
35. C. Gutt, T. Ghaderi, V. Chamard, A. Madsen, T. Seydel, M. Tolan, M. Sprung, G. Grubel, S.K. Sinha, Phys. Rev. Lett. **91**, 179902 (2003).
36. M. Paulus, C. Gutt, M. Tolan, Phys. Rev. B **78**, 235419 (2008).
37. R.A. Pushkarova, R.G. Horn, Langmuir **24** 8726 (2008).